Quantifying Impacts on Remote Photogrammetric Inspection Using Unmanned Aerial Vehicles

Dayi Zhang*, Robert Watson, Gordon Dobie, Charles MacLeod, Aamir Khan, Gareth Pierce

Centre for Ultrasonic Engineering, University of Strathclyde, 204 George Street, Glasgow, G1 1XW, UK

Corresponding Author. Email Address: dayi.zhang@strath.ac.uk

Abstract

Remote photogrammetric inspection is a Non-Destructive Testing method used to quantify surface integrity and detect external discontinuities. The mobility and size of an unmanned aerial vehicle (UAV) offer the flexibility to quickly deploy remote photogrammetric inspections for large-scale assets. In this paper, the results of a photogrammetric inspection are presented as a 3D profile, reconstructed from UAV captured images. Experiments were conducted indoors using a wind turbine blade section obtained from a recently decommissioned asset. The naturally occurring surface features representative of environmental wear were augmented with a small number of artificial features to aid in the visualisation of inspection quality. An autonomous UAV system for photogrammetric inspections is demonstrated and the influence of image parameters such as environmental light levels, motion blur and focal blur quantified in terms of their impact on the inspection accuracy. Over the range of parameter values studied, the poorest scenario was observed to cause a degradation in reconstruction error by a factor of 13 versus the optimal. Reconstruction quality when employing a laser range scanner to maintain standoff distance relative to the object during flight was also investigated. In this schema, the controller automatically generated a real-time adaptive flight path to follow the outer profile of the wind turbine blade and, consequently, demonstrated improved image quality during close-range inspection of an object with complex geometry. Inspection accuracy was quantified using the error of the photogrammetric reconstruction as compared to a model acquired using independent metrology equipment. While utilising the laser-based adaptive path, error in the reconstructed geometry was reduced by a factor of 2.7 versus a precomputed circular path. In the best case, the mean deviation was below 0.25 mm. Instances of wind turbine blade damage such as edge crushing, surface imperfections, early stage leading edge erosion were clearly observed in the textured 3D reconstruction profiles, indicating the utility of the successful inspection process. The results of this paper evaluate the impact of optical environmental effects on photogrammetric inspection accuracy, offering practical insight towards mitigation of negative effects.

Keywords: Autonomous Photogrammetric Inspection; UAV; Accuracy Quantification

1. Introduction

Photogrammetric inspection, a form of visual inspection, is a non-destructive testing method that uses a camera to evaluate the surface condition of industrial assets. The technique and its related algorithms are moving forward, and range of research interests for its Non-Destructive Testing (NDT) applications are growing [1]. The progression can be attributed to the benefits of photogrammetry, such as low cost, fast speed and no requirement for physical contact. Compared with some conventional NDT sensors which measure at discrete points, photogrammetry provides an opportunity to perform a full-field measurement, wherein an informative overview is produced at a relatively high speed albeit with no internal structural detail. Moreover, photogrammetry can achieve more frequent measurement, reducing workload and health risk to inspectors [2].

The application of the photogrammetric technique to wind turbine blade monitoring has been growing since the 1996 work by J.C. Sabel [3]. This deployed two cameras, affixing reflective stickers to the turbine tower and its 10 m diameter blades to measure vibration whilst the system was operating. A projector-based system has similarly been applied for turbine blade fatigue testing [4]. Additionally, the photogrammetric technique has been utilised to measure the dynamic characteristics of a wind turbine blade [5]. Therein, authors demonstrated a system equipped with two high-speed cameras to capture blade movement.

An Unmanned Aerial Vehicle (UAV) is a pilotless flying vehicle and provides flexibility to undertake many challenging access problems. A UAV with photogrammetric payload enables technicians to inspect the surface of the large-scale assets [1]. In existing literature, UAVs have been utilised in various inspection tasks, such as building surveys [6], detecting discontinuous on power cables [7], inspections of a nuclear waste storage container [8] and evaluating structural conditions of bridges [9]. J. Seo et al presented a UAV-based approach for the inspection of a timber bridge [10]. In this work, the authors concluded that the image quality, and thus the accuracy of the resulting inspection, is constrained by factors such as UAV platform positioning instability and camera exposure parameters. Similar researches on UAV-based photogrammetric inspections for bridges [11]–[13] and other infrastructure [14] have been conducted in the United States. These articles describe a methodology for the assessment of image quality prior to the inspection stage to improve the accuracy of the inspection. S. S. Mansouri et al. described a UAV swarm approach to inspect an outdoor sculpture where the UAVs were navigated by stereo camera-based system [15]. The current state-of-art of the UAV inspection of wind turbine blades focuses on improving inspection accuracies, such as developing algorithms to detect defects from offline pictures [16] and investigating mechanical approaches for contact measurements [17] [18]. These conventional photogrammetric

approaches typically present inspection results in multiple separate images, which struggle to convey position and location information.

By contrast, 3D photogrammetric reconstruction is the process of generating a computer model of the 3D profile of an object from a set of 2D images and implicitly displays surface feature locations. This process can be classified into three main categories depending on the type of image acquisition equipment used: Single Camera-based methods, RGB-Depth sensor-based methods and Multicamera network-based methods. An overview of these methods and their respective sub-categories is depicted in Figure 1, where the depth of nodes reflects an increasing accuracy. As shown in the figure, Structure from Motion (SfM) [19], Multiview Stereo [20] and Visual SLAM (Simultaneous localization and mapping) [21] all use a single camera to reconstruct the 3D models. The technique of SfM involves extracting the unique features from a collection of 2D images and matching these features to estimate sparse scene geometry and camera positions. The sparse point cloud and estimated camera positions generated by SfM are further processed by application of Multiview Stereo algorithms, which calculate densified point clouds to render an accurate 3D geometry. Visual SLAM reconstructs the large-scale targets and camera surroundings in real-time. However, real-time processing requires enhanced computational power and can come at the expense of reconstruction accuracy. An RGB-Depth sensor outputs a conventional RGB image alongside a depth image. Depth Fusion [22] [23] uses this information, combined with the traditional RGB image features to reconstruct a 3D model. Similar to the visual SLAM, RGBD SLAM [24] uses the camera outputs to reconstruct the scene in real-time. Multicamera based methods [25] use the images captured by multiple cameras placed at various pre-planned positions. Compared with the single camera solutions, multiple cameras with known camera positions do not require mathematical approaches to estimate camera poses, which improves the reconstruction accuracy. Considering the physical limitations of the UAV and accuracy requirements of the inspections, SfM and Multiview Stereo are utilised in this paper.

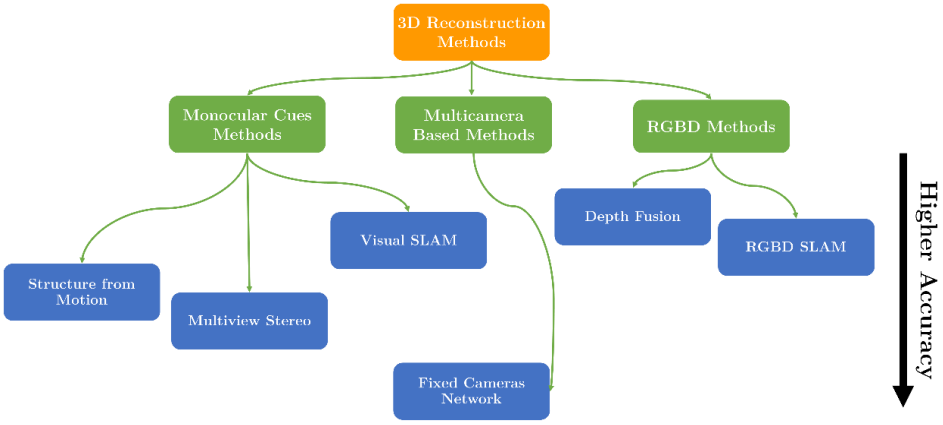

Figure 1 Approaches for 3D Reconstructions

Implementations of these 3D reconstruction algorithms are seeing utilisation for digitising archaeological art [26] but also for UAV indoor navigation [27]. During NDT inspections, a textured 3D model can be built up from multiple images and so provide a more contextual assessment of the target object. By estimating the approximate location of each image, the reconstruction progress represents a feasible approach to quickly localise the defects, especially on assets with complex or very self-similar geometry. Compared with inspections composed of isolated images viewed offline, 3D photogrammetric inspection provides results with intrinsic position and location information that are of great utility in the production of meaningful surface condition evaluations. The inspection process when using this technique requires a UAV equipped with a photogrammetric payload to manoeuvre around the target object and take images in different positions and orientations to ensure the entire object surface has been observed sufficiently for reconstruction. Such an approach has been utilised on the inspections for bridges, structures and buildings [1]. As documented in [28] and [29], the accuracy of the 3D photogrammetric inspection results is impacted by the image quality, UAV movement, environmental light levels, motion blur and distance to the object.

2. Aim and Objectives

This paper demonstrates and quantifies the parameters influencing the accuracy of a close-range photogrammetric inspection using an autonomously controlled UAV. A laser scanner aided inspection of a wind turbine blade with complex geometry will be presented. The 3D profile generated when flight paths are assisted by laser data is investigated regarding the accuracy and detail of reconstructed features.

Section 3 provides an overview of the autonomous UAV inspection system and experimental setups utilised in this paper. Section 4 quantifies and analyses the impacts of quality parameters affecting UAV deployed photogrammetry. Section 5 presents an inspection with a laser-based flight trajectory and describes the impacts of UAV standoff distance. Section 6 presents a discussion based on the experimental results from Section 4 and Section 5. Finally, in Section 7, the paper is concluded with a discussion of results and the insights gained from the work.

3. Overview of the Experimental Inspection System

The inspection system utilised in this paper (as shown in Figure 2) is composed of: an AscTec Firefly UAV [30], a FLIR machine vision camera CM3-U3-50S5C-CS [31] with an 8 mm, F2.4, 57.8° field of view lens [32] and a Hokuyo URG-04LX laser scanner [33]. This photogrammetric payload is mounted on the UAV and captures 4

MegaPixel (MP) raw images at 2 Hz with the camera lens manually adjusted for optimum focusing at a set distance. Sensor communications and image acquisition are processed by the UAV's onboard Intel Core2 Duo Computer (running a Linux-based Operating System). The raw images, captured during the UAV flight, are saved on this computer, then exported to an offline computer for further reconstruction processing.

The UAV was autonomously stabilised and guided to follow inspection trajectories generated by a customised controller running on the off-board, ground-based workstation and updated every 50 ms. Onboard, the aircraft's flight controller is based on a closed-loop Proportional-Integral-Derivative (PID) architecture [34] and adjusts the UAV attitude depending on the difference between the desired and actual poses.

While the UAV described here is designed to be capable of outdoor inspections, the experiments demonstrated in this paper were undertaken within a laboratory environment, wherein GPS signals are unavailable to provide a reliably accurate position for UAV tracking and navigation. Consequently, a high-accuracy photogrammetry-based Vicon position measurement system is used as a replacement for GPS when performing indoor navigation. This system comprises twelve optical cameras and tracks the six degree-of-freedom UAV pose at 100 Hz. The Vicon system positional accuracy error was quantified below 0.51 mm when locating a stationary target [35], but rises to 2 mm when tracking a moving object [36].

The Hokuyo laser range scanner [33] mounted atop the UAV is utilised for mapping the target and other local infrastructure in front of the UAV. The scanner has a 240° field of view with 0.35° angular resolution, samples data at 10 Hz and has a mass of 160 g. It can conduct measurements within a functional range between 60 mm and 4095 mm and is accurate to ± 10 mm while the distance to the object is within 1 m. The errors increase to 1 % of measured value when observing targets at a distance between 1 m and 4 m. Researchers have previously demonstrated this accuracy when measuring the distance to industrial samples [37]. Here, the sensor outputs are used to maintain the UAV standoff distance and generate adaptive flight path during the inspection process.

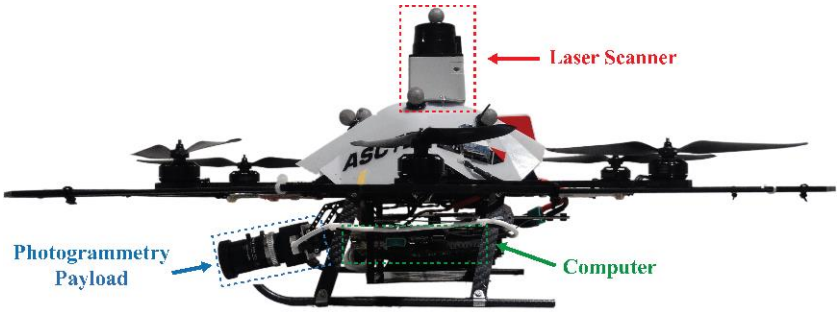

Figure 2 AscTec UAV with an onboard computer, camera and laser range scanner

The inspection target utilised in this paper is a 3.1 m tall section of wind turbine blade, a decommissioned part of a Gaia–Wind turbine [38]. The blade section is mounted vertically and tapers from 619 mm wide at the bottom to

386 mm wide at its highest point. Typical wind turbine blade damage [39], [40], including edge crushing, surface imperfections, early stage leading edge erosion and other edge damage can be observed on the blade surface (as in Figure 3). Once initiated, such damage will be extended by environmental conditions encountered during daily operations. If not adequately addressed as part of an operation and maintenance strategy, loss of the protective surface layer can allow water penetration and ultraviolet degradation that will cause secondary defects and increase the risk of structural failure [39]. Though scuffs and cracks are observable on the surface, to better quantise the performance of the 3D reconstruction and aid procedures when adjusting the camera focus, the blade surface has undergone some prior preparation. Ten 6.5 mm dots and a textured yellow 20 mm tape were affixed to the middle section of the surface (as in Figure 3), whereas the top and bottom sections of the blade remained in their original state. Since the reconstruction errors on the middle, top and bottom were found to be identical in magnitude (as shown later in Figure 15), it can be surmised that such surface enhancements have had minimal effect and the sample is still indicative of real inspection scenarios.

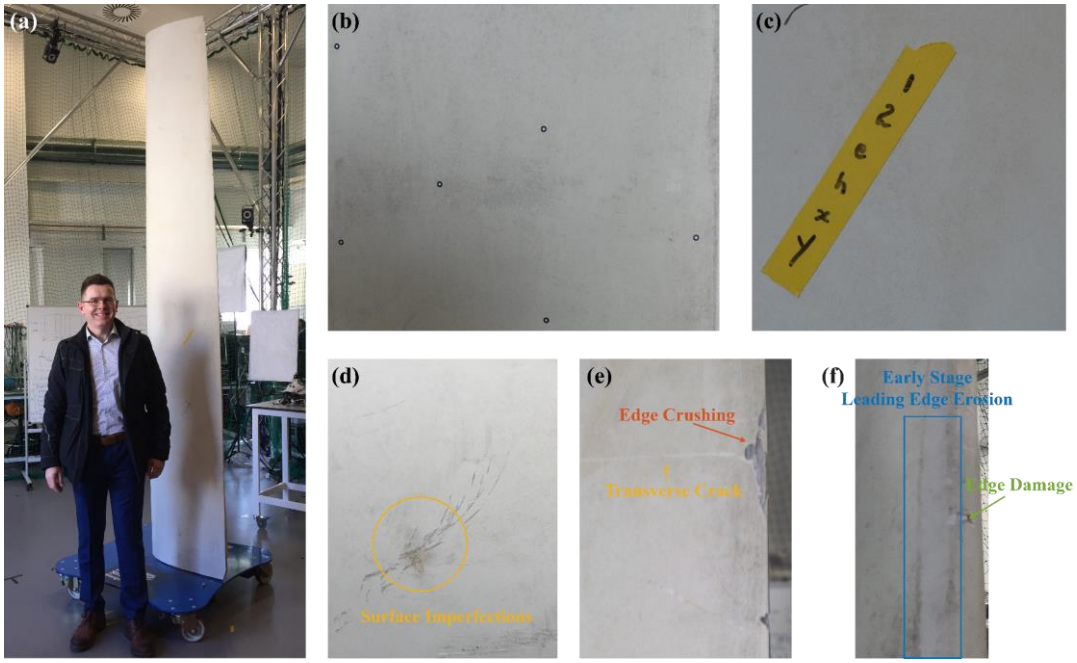

Figure 3 (a) Wind turbine blade for inspection (b)(c) dots and texture features added to the blade surface (d)(e)(f) Existing surface Imperfections, edge damages and transverse cracks on the blade surface

The 3D reconstruction is conducted via Agisoft PhotoScan [41], a commercially available stand-alone software product which performs photogrammetric processing of digital images and generates 3D spatial data. The software assumes the images are captured from a series of cameras in various unknown positions. It calibrates the camera using Agisoft proprietary algorithms [41] before extracting and matching the features from consecutive images to estimate their relative poses. Point clouds, meshes and textured reconstructions are built in sequence to create a detailed 3D profile.

To ascertain the accuracy of the inspection results, a reference CAD model was captured using the GOM ATOS Triple Scan system. The model generated by the GOM system has been shown to be highly accurate, with nominal surface deviation below 20 μm [42]. Complete mesh data from PhotoScan was imported into GOM Inspect, software used for comparison with the reference CAD model. Note that because monocular photogrammetry is a dimensionless technique and, as such, the scale factor is unknown during the reconstruction process, the output from the software does not contain the absolute sizing of the model [43]. Therefore, prior to comparing the models, a scaling factor relating the Agisoft mesh and to the ground truth model coordinate system is required. An initial value was obtained by identifying two distinctive points from the GOM mesh in the reconstruction then setting their separation accordingly before fine-tuning by minimizing the surface deviations between reconstructions. Applying this factor and conducting the model comparison, the standard deviation, mean error, peak-to-peak error and a deviation map can be obtained from GOM Inspect. The standard deviation represents the noise level on the model surface, while mean error and peak-to-peak denote the geometric difference.

Figure 4 Reconstructed 3D model for the wind turbine blade

Figure 4 shows an example of a reconstructed model from the Agisoft PhotoScan software. In the best-case scenario, reconstructions achieved by this UAV system for photogrammetric inspection present with the mean error below 0.25 mm relative to the GOM reference model. Peak-to-peak error and standard deviation are below 4.3 mm and 0.92 mm, respectively.

3.1. Experimental Setup

The main considerations dictating camera selection for remote airborne inspection are the dimensions, mass, resolution, frame rate and communication interface of the sensor. Dimensions and mass are restricted by the UAV hardware's payload limitations. Frame rate and communication interface constrain the software application that may be deployed and ultimate image processing speed during data acquisition. Higher resolution cameras offer the capability to capture more detailed surface features. There exists a significant repository of institutional experience with the communication interface employed by the Chameleon3 following its deployment within other previous research projects [44][45]. These works have additionally demonstrated that camera series to be an effective compromise between the above parameters. Hence, the camera with the highest specifications and resolution in the Chameleon3 series has been selected as the photogrammetric payload for the UAV inspections detailed here. The camera nominal sample rate is 35 frames per second. However, due to hardware limitations associated with the data transfer between the camera and the UAV's onboard computer, the actual frame rate achieved is 2 Hz. Image compression is disabled during the inspections to prevent the introduction of associated image distortions and artefacts.

The focal length of such a lens dictates the camera field of view and so has significant impact on the remote visual inspection process. A short focal length provides a wide field of view, reducing the number of images required to cover a given surface area but diminishing the ability of the images to accurately resolve small features. Selecting a lens with a wider aperture enables more illuminance to enter the camera, improving the image brightness. The Computar MPW2 lens series is designed for compatibility with cameras using 5 MP and 2/3" sensors. Since the UAV inspections require the imaging of a large area of the structure, M0824-MPW2, the smallest focal length in this series (8 mm), was selected for use and mounted with the Chameleon3 camera on the front of the UAV. The lens however has no capability for automatic focus adjustment. This, therefore, was set manually by placing the craft at the required standoff distance to the target object and incrementally adjusting focus to acquire the optimum surface texture sharpness.

The Hokuyo laser range scanner URG-04LX has been implemented in many research platforms. Authors of existing literature have characterised the performance of this scanner [46] and demonstrated its accuracy when measuring the distance to industrial samples [37]. The results disseminated in these publications demonstrate the sensor's aptitude for distance measurement during the NDT inspection process and justify its employment here.

In this paper, three parameters impacting inspection accuracy are quantified: environmental brightness, image motion blur and focal blur. These parameters have been identified as the most common sources of the error during UAV inspections and are known to have direct impact on the image quality and ultimate inspection accuracy [28].

The impacts of these parameters are quantified and detailed in subsequent sections. It is found that these impacts can be lessened by appropriate experimental setups and UAV flight paths, which will be demonstrated by empirical results. Multiple experiments were undertaken with different environmental lighting conditions, different standoff distances and a selection flight paths generated by the laser scanner and are quantified against the GOM reference model.

4. UAV Inspection Image Quality Parameters

4.1. Environmental Brightness Condition

Image brightness is one of the parameters influencing image quality and reconstruction accuracy [28]. The images captured under low light intensity lost the detailed features of the target surface leading to the failure of image feature extraction algorithms and hindering the reconstruction process. Undertaking the experiments in a laboratory environment allows the ambient light levels to be fully controllable by the use of diffuse supplementary lighting. Within the laboratory and in the absence of additional illumination, the light intensity was measured by a calibrated lux meter as 65 ± 5 lx. To quantify the impact of the light intensity on reconstruction accuracy, six additional 135 W lights with a colour temperature of 5500 K were set-up at suitable locations around the wind turbine blade, as shown in Figure 5. These external lights introduce additional illumination of the blade surface and permit increase in environmental light levels by a factor of three, from 65 lx to approximately 200 lx. By comparison, the ambient environmental light measured by using the lux meter outdoors on a cloudy day is around 2000 lx. This laboratory lighting environment, therefore, provides a good facility to investigate the impact of the environmental brightness parameter on reconstruction in such conditions as may be encountered in practice during markedly poor weather.

Figure 5 External lights Setup

When operating within an environment with poor light intensity, increasing the camera shutter time allows more illuminance to fall onto the camera sensor and so produces brighter images. However, slower shutter speed introduces more motion blur to the images owing to small motions of the UAV platform intrinsic to the nature of such aircraft. In contrast, decreasing shutter time can reduce the blur but sacrifices image brightness. Motion blur is also a source of reduced image quality and strongly influences the inspection accuracy, obscuring visual features and hindering the functionality of algorithms for feature detection employed in the reconstruction progress. Further details of these effects will be provided in Section 4.2. It is noted that under ideal direct sunlight conditions outdoors, the shutter time can be reduced to as low as 1 ms during inspections to mitigate the motion blur issue. This, however, represents an uncontrollable environmental influence that cannot be relied upon in practice frequently necessitating the deployment of other compensatory methods such as those elucidated herein.

This experiment is designed to quantify the impact of the lighting conditions and shutter speed on the reconstructed models. The UAV flight path in the experiment was a pre-planned circular path, taking the UAV a complete rotation around the wind turbine blade section before dropping down and performing the next loop until the full vertical distance of the sample has been covered, all while capturing images at regular time intervals. In this scenario, the camera shutter time was set to be 30 ms, representing the exposure time that captured the images of the best quality in the presence of the additional lighting. In this trial three image sequences were recorded. The first image sequence was captured under the environmental lighting conditions obtained with the six additional lights, the second and third were captured without these lights at the laboratory ambient light level. In the third trial, to demonstrate the impact of shutter time on reconstruction accuracy and create similar image brightness to the well-lit trial, the camera shutter speed was changed to 60 ms. Figure 6 displays raw images taken at similar locations for comparison between the three image sequences, captured under different light intensity and varying shutter speed. The deviation maps and the errors of reconstruction models under each of the three setups are illustrated in Figure 7 and Table 1. The quality of the images from the inspections with three setups are plotted in Figure 8. The image qualities from each trail are quantified by using the matching feature density metric, as explained below. A fourth image sequence using the 60 ms exposure time and additional lighting is not conducted as this leads to overexposed images from which no meaningful results may be extracted.

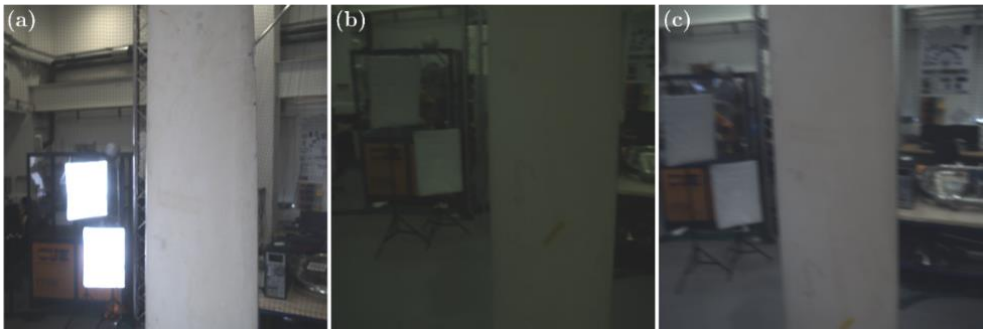

Figure 6 UAV captured images under: (a) 30 ms shutter with supplementary lighting, (b) 30 ms shutter without supplementary lighting, (c) 60 ms shutter without supplementary lighting.

Table 1 Reconstruction errors from the inspection with different environmental brightness conditions

	Mean Error (mm)	Standard Deviation (mm)	Peak-to-peak Error (mm)
30 ms shutter with light (Light = 200 lx)	0.3853	1.56	13.56
30 ms shutter without light (Light = 65 lx)	0.6493	2.46	68.00
60 ms shutter without light (Light = 65 lx)	0.4571	1.97	22.91

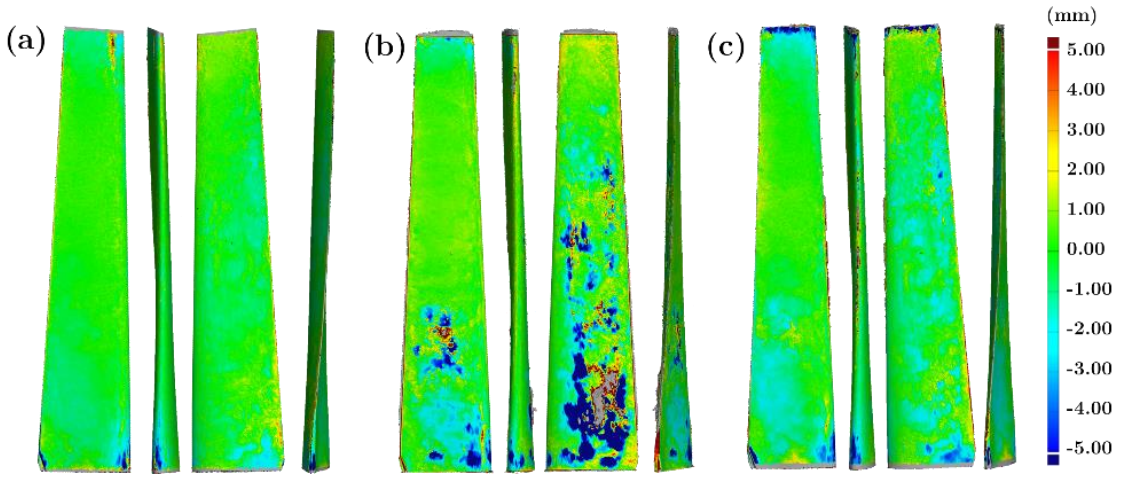

Figure 7 Deviation maps of the reconstruction model captured in different parameters: (a) 30 ms shutter with supplementary lighting, (b) 30 ms shutter without supplementary lighting, (c) 60 ms shutter without supplementary lighting.

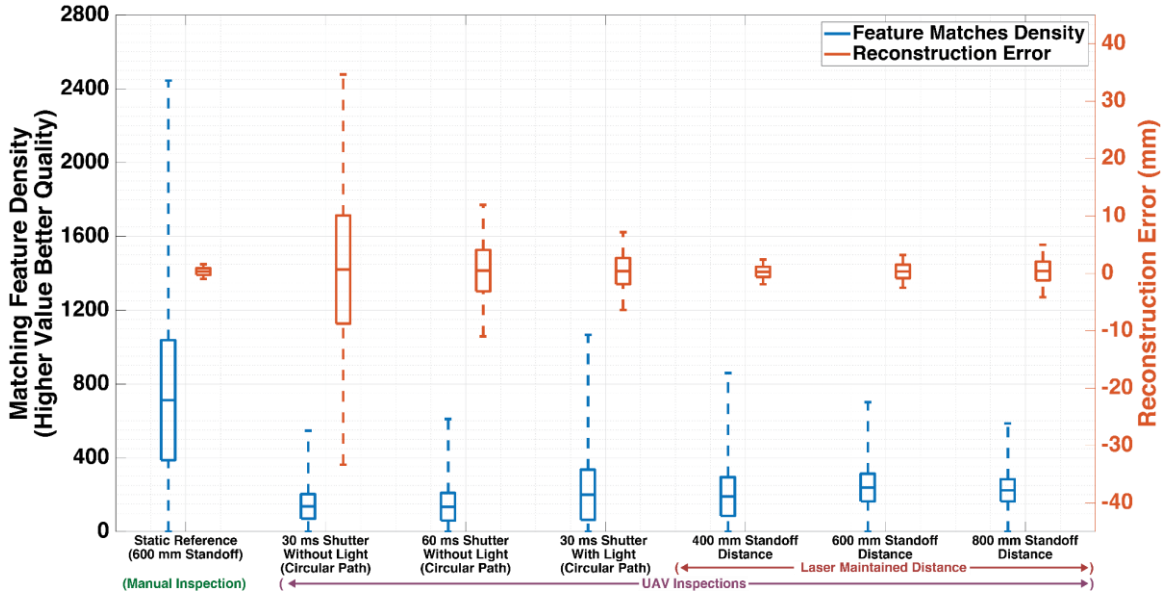

Figure 8 Image quality and reconstruction error under different experimental setups. The reconstruction errors are plotted by using the mean errors and standard deviations.

Image feature matches are the key factors in the 3D reconstruction process. Correlation between increased feature matches and a better quality of reconstructed model has been previously established [19]. Similarly, the percentage of image overlap is well recognised to influence the number of feature matches between consecutive images. Matching feature density is thus introduced as a comparative metric describing the number of the matched features in an overlapping region and quantitatively assess how this impacts the quality of the final reconstruction. It is calculated by dividing the number of the matched features between two subsequent images by the area of their overlap, with this area expressed as a percentage of the full image size. Using the matching feature density to quantify the quality of images obtained during autonomous UAV inspections, image sequences captured with different optical setups can be directly compared and evaluated. Higher density implies that an image had more matching features and is thus indicative of better image quality.

The image quality distribution across all image sets (as presented in Figure 8) shows that those captured under the lowest light intensity, without supplementary external lighting had the worst quality. Correlating with the intuitive outcome, the average quality was improved with the increase of camera shutter speed and environmental light intensity.

As discernible from the data presented in Table 1, the model reconstructed from the images captured under 30 ms shutter speed, in relatively dark conditions (65 lx), had 60 % worse geometry alignment and around 63 % larger standard deviations than the model from the images captured with the same shutter speed at 200 lx. Compared with the model acquired in bright conditions (Figure 7 (a)), the mesh acquired in dark conditions contained a large discontinuity in both the blade's front and rear surfaces (Figure 7 (b)). Discontinuities and misalignment were

additionally observed at the bottom section of the mesh due to the loss of image features in the low light environment and the consequential inability of the reconstruction algorithms to accurately extract the blade structure in these regions.

Under the same lighting conditions, the increased 60 ms shutter time of the third data set improved the image brightness by 40 %, leading a 30 % reduction in the mean error (from 0.65 mm to 0.46 mm) and 20 % reduction in standard deviation (from 2.46 mm to 1.97 mm) when compared to the second trial. Additionally, as presented in Figure 7(c), the PhotoScan software generated a complete mesh for the wind turbine blade. However, the model standard deviation error was still over 20 % larger than in the case using the images with shorter shutter time in a brighter environment. As described previously, the error is identified as a result of additional motion blur, caused by the UAV movements and compounded by the slower camera shutter speed. These effects coupled with feature distortions, manifest as a change in peak-to-peak error of 9.35 mm.

4.2. Motion Blur

Motion blur appears from the UAV movement during the camera exposure and is related to the UAV flight stability and velocities in all six degrees of freedom: rotational and translational [29]. It is intrinsic to the nature of the UAV platform owing to its subjection to disturbance by miniature air currents and orientation sensor noise. To investigate the impact of the motion blur on the reconstruction accuracy, the inspection was initially undertaken by the UAV operating with full autonomous control to eliminate any disturbances introduced by a human pilot. For comparison, a data set was acquired with the camera statically mounted and positioned at a standoff of 600 mm to the blade surface to provide “best-case” image capture conditions in the absence of the UAV movement and motion blur. These experiments were undertaken with the same enhanced illumination from the external lights as in Section 4.2 allowing the camera shutter time to be set at 30 ms throughout.

As shown in Figure 8, the images captured during the manual inspection had better qualities than the images taken during the UAV flight with the same 600 mm standoff. The reconstruction accuracies listed in Table 2 show the motion blur from the autonomous UAV slightly increased the mean alignment error. Moreover, the addition of motion blurring leads to the increase of the standard deviation and peak-to-peak error by almost a factor of two. Motion blur causes distortions in the image and so induces error in the reconstruction results. However, due to the nature of UAV flight, these motion blur effects cannot be fully eliminated, only compensated for by the informed selection of camera settings (e.g. faster shutter speed) and a higher-performance flight controller to counteract the UAV instabilities.

Table 2 Reconstruction errors from the UAV inspection and manual inspection

	Mean Error (mm)	Standard Deviation (mm)	Peak-to-peak Error (mm)
Manual Inspection (600 mm Standoff Maintained by Laser Scanner, Light = 200 lx)	0.2956	0.71	2.55
UAV Flight (600 mm Standoff Maintained by Laser Scanner, Light = 200 lx)	0.3098	1.29	5.09

4.3. Focal Blur

The Depth of Field (DoF), or focus depth, is the distance between the nearest and furthest positions relative to the camera at which an object located will begin to exhibit an unacceptable loss of sharpness in its captured image [47]. The remainder of the scene behind and in front of these two positions is distorted and exhibits focal blurring. In the context of photogrammetric inspections, focal blur appears when the camera is positioned such that the target object is located outside the depth of field. This distorts the appearance of the image features relied upon during reconstruction and so produces a malformed 3D representation, degrading the inspection quality and increasing the possibility of asset condition misdiagnosis when examining surface discontinuities [29]. The camera utilised to conduct photogrammetric inspections presented here is adjusted to be focused on the blade surface to achieve the best sharpness at a given standoff distance. Conventional UAV-based photogrammetric inspections are performed using a high-resolution camera at a large standoff distance to avoid the risk of collision. The width of the depth of field increases with the camera standoff distance [47], therefore, cameras in conventional inspections have a broader depth of field and the ability to capture images with less focal blur. However, inspections conducted at close proximity grant opportunities to capture more detailed surface features. The applications presented in this paper were examples of such close-range inspections, wherein the UAV on which the camera was deployed was positioned at a standoff distance of 600 mm to the blade surface. This leads to a comparatively shallow depth of field. The depth of field is around 331.8 mm with 600 mm UAV standoff distance, calculated by Equation 1 [47].

$$DoF = \frac{2cN(D+130)^2 f^2}{f^4 - c^2N^2(D+130)^2} \quad (1)$$

Where c is the camera circle of confusion diameter limit (0.008 mm), f represents the camera focal length (8 mm), D is the UAV standoff distance to the outer perimeter of the area swept by the aircraft's rotors and N is the lens aperture f-number (2.4). Note that the 130 mm in this equation is the distance between the UAV outer perimeter and the camera.

Thus, the UAV is required to maintain position within a distance of 470 to 802 mm to the surface of interest in order to capture images with acceptable sharpness.

To demonstrate the impact of standoff distance on image quality, photographs of an ISO 12233 Test Chart [48] were taken at various standoff distances using the Chameleon3 camera and Computar lens. The test chart has abundant textures and is designed specifically to test the camera resolution and focal point. In the experiment, the camera is focused at 600 mm UAV standoff and then displaced to a range of positions along the surface normal vector. Images are captured from a standoff of 300 mm to 1000 mm in 100 mm increments. Figure 9 depicts the test chart images, taken from 300 mm and 600 mm standoff distance. Compared with the image captured at 600 mm standoff (as in Figure 9(b)), the image from 300 mm distance is much blurrier and out of focus.

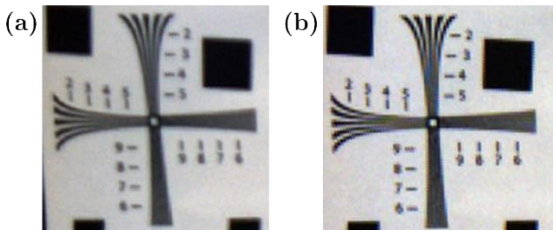

Figure 9 Captured Test Chart (cropped to show the area of interest), while the camera is focused on 600 mm standoff distance (a) camera, was placed at 300 mm standoff (b) camera was placed at 600 mm standoff

An open source blur metric function, evaluated within the MATLAB data processing software environment, was utilised to quantify the degree of blur present in the captured images. This blur metric function described by Crété-Roffet et al [49] is based on a percentage similarity comparison between the original image and image after passing through a low-pass filter and functions as a relative comparison between two images of the same subject. The quality of the images captured at different standoff distances evaluated using this metric is plotted in Figure 10. A higher value of blur index implies poorer image quality. As expected, the camera captured the best quality in the focal point and quality became worse with the standoff distance away from the focal point.

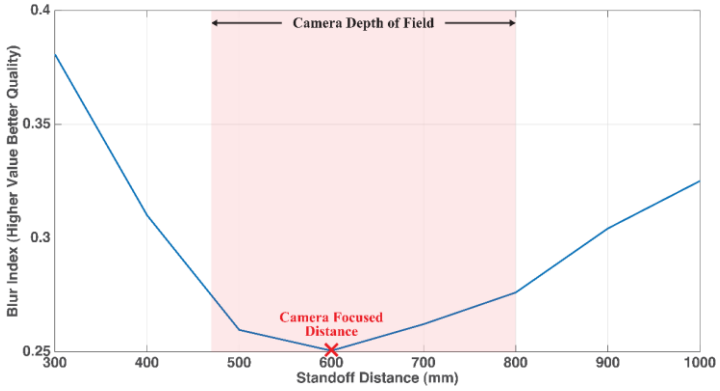

Figure 10 Image qualities at various standoff distances (camera is fixed focused at 600 mm)

5. UAV Flight Path Parameters

5.1. Laser-based Flight Path

The results presented in Section 4.3 illustrate the relationship between the standoff distance and image quality. To acquire precise photogrammetric inspection results, the target object in the images is required to be resolved with sufficient sharpness to extract features and infer 3D structure. Therefore, the UAV standoff distance needs to be maintained at a level that places the inspection target within the camera lens' depth of field. The flight trajectory is thus required to track the asset's geometry so as to maintain appropriate standoff distance and ensure the camera focal point lies as close as possible to the asset surface.

There are two methods to maintain the standoff distance and guide the UAV to follow the target geometry. Firstly, a pre-planned path can be programmed and assigned by utilising an existing 3D mesh of the inspection scene. However, this method is less robust because the flight trajectory is hardcoded and so relies on both an accurate 3D model and strong disturbance rejection in the UAV controller. In a laboratory environment, the target object can be moved to a known place for inspection, typically the centre of the measurement flight volume, and a flight trajectory generated accordingly. Difficulties associated with locating the planned flight trajectory relative to the physical structure and an increased likelihood for environmental disturbances mean that this method is not suitable for inspection of in-service assets. It is insufficiently robust to provide safe and reliable inspections when flying under autonomous control and in close proximity to industrial plant items.

A more adaptive second method entails applying a miniature laser scanner to provide real-time feedback control. The laser scanner is equipped aboard the UAV to measure the displacement to its surroundings and the target object. A curve fitting algorithm is utilised to process the raw data output and compute the standoff and orientation errors in real-time by fitting a plane to the closest part of the structure. Compared with the pre-planned path, this method does not require knowledge of the target model and represents a much more feasible approach to avoid collisions during close-range inspections. In this method, measured distances are fed into the UAV controller to maintain the standoff distance. Alignment errors between the UAV yaw angle and surface normal vector are calculated to adjust the UAV orientation in real-time. This can guide the UAV to follow the object geometry and readily maintain position where the target object lies within the camera's depth of field. To demonstrate the ability of this strategy to minimise the negative impact of focal blurring, empirical trials are conducted where the inspection path was compensated to follow the adaptive trajectory, computed in real-time using data from the laser scanner.

An inspection with pre-planned circular path was utilised for comparison with the adaptive path. The circular path comprises nine circumferences with fixed distances to the blade centre varying in accordance with altitude, owing

to the tapering of the blade profile along its length and its vertical mounting. The UAV starts circular manoeuvring around the top of the blade and finishes at 0.7 metres above the ground to ensure complete coverage the whole blade's surface area while avoiding collisions. Upon completing each circumference, the altitude is decreased by 300 mm and the UAV commences travel around the next layer's circumference. This layer altitude separation distance is selected to ensure sufficient vertical image overlap in accordance with the camera field of view. Because of the geometry of the blade, the radius of the top circular path is 1100 mm and increases in 50 mm steps as the path progresses to lower altitudes.

Using this circular path planning method, the standoff distances vary between 522 mm and 1045 mm, owing to the aerofoil cross-section of the blade. Comparatively, the camera focal range is between 470 mm and 790 mm. Therefore, some focal blur is unavoidable in the images captured using this path when deploying a fixed focus camera. Both the inspections with a pre-planned path and laser-based path were undertaken with the additional external lighting used previously, permitting the camera shutter time to be set at 30 ms.

When comparing the circular and laser-based paths, as in Figure 11, the most prominent difference is the standoff distance between the UAV and the targeted inspection asset (i.e. the wind turbine). The circular path entails a varying standoff distance (between 600 and 826 mm) owing to its nature as a pre-planned heuristic path, generated with minimal a priori knowledge. Inspections relying on such algorithms will experience focal blurring in the images taken at points where the flight path diverges most from the inspection surface geometry, granting a significant degradation in cases of complex asset geometry. In contrast, given the same level of a priori knowledge, the laser-based adaptive control strategy can, in real-time, ensure that the camera remains at the correct standoff distance to retain the asset surface within the well-focused depth of field. Thus, regions of increased focal blur are avoided, and the inspection accuracy is improved.

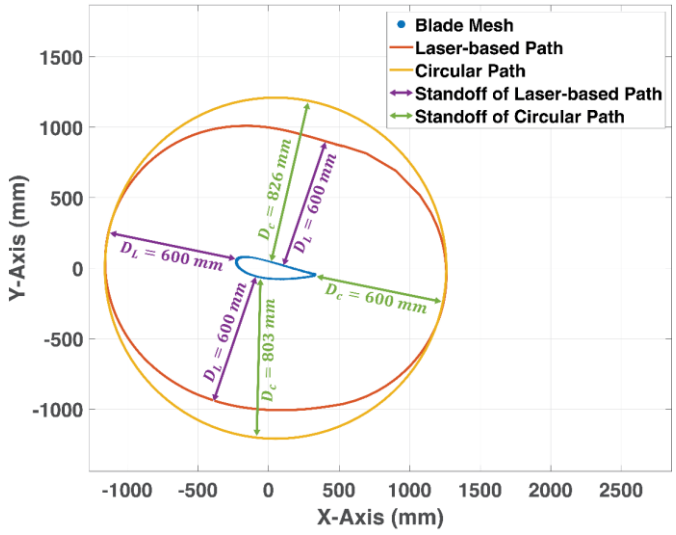

Figure 11 Comparative diagram of the circular and laser-based paths when executed about the aerofoil cross-section of a wind turbine blade.

To demonstrate the accuracy of the laser scanner maintained distance, an idealised flight path is generated in MATLAB based on the highly accurate reference model obtained using the GOM ATOS Triple Scan system. The path is generated by slicing the mesh of the turbine blade at regular height intervals, forming a perimeter at each interval, then expending these perimeters to the correct standoff distance. This defines the ideal flight trajectory with 600 mm standoff distance to the blade surface. The UAV flight path as executed in both cases is recorded utilising the Vicon tracking system (as indicated in Section 3.1) and is plotted in Figure 12. Path standoff errors are calculated between the desired path and executed path and plotted in Figure 13, illustrating the performance of each strategy. The distribution of error magnitudes demonstrates that when utilising the adaptive path, the UAV equipped with a laser scanner successfully placed the sample surface within the camera's depth of field and was able to maintain this positioning while encircling the component under examination.

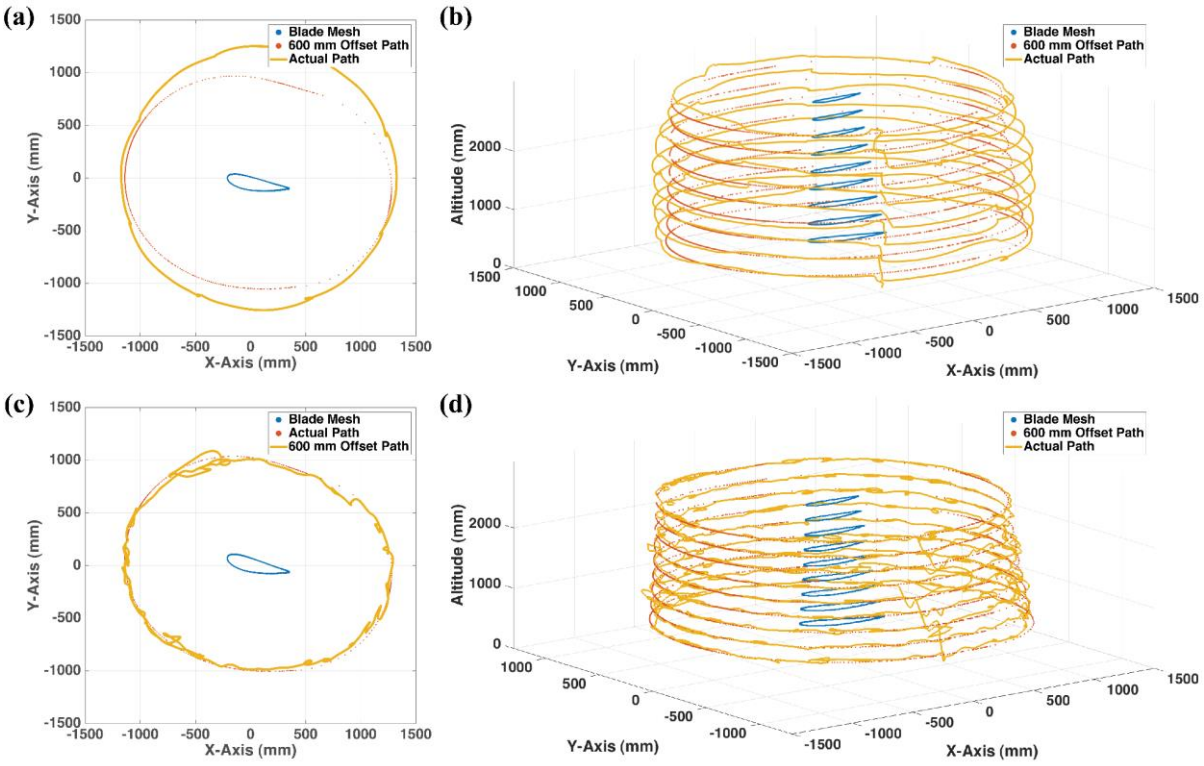

Figure 12 This figure includes slices of the blade mesh (blue), a MATLAB generated path with 600 mm standoff distance (red) and executed path (orange). (a)(b) pre-planned circular trajectory (c)(d) laser-based adaptive trajectory

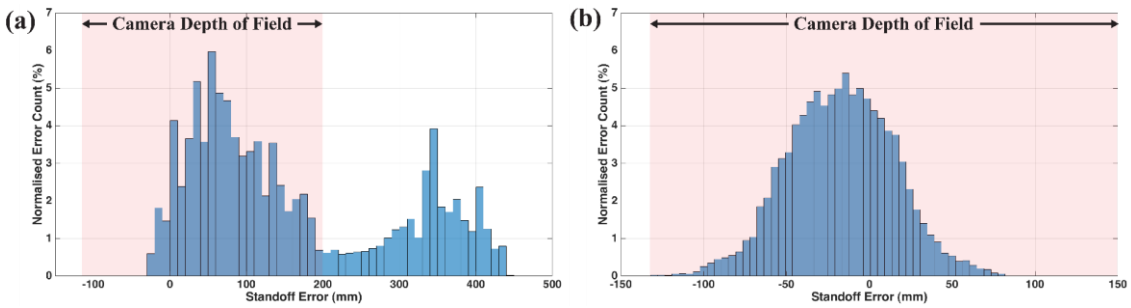

Figure 13 Histogram of the error between MATLAB generated path and UAV executed path (a) pre-planner Trajectory (b) laser-based Trajectory

The raw images shown in Figure 14 were captured when UAV was inspecting similar areas of the blade with pre-planned trajectory and laser-based trajectory. The differences between these images visually demonstrate how the inspection with laser-based path was able to better maintain focus on the blade surface. More focal blurring is found on the images captured on the pre-planned circular path, the source of which is identified as the varying standoff distance during the inspection. Compared with the images from the pre-planned circular path, the textures and features on images captured during the laser-based inspection are sharper and more detailed leading to better image qualities, as shown in Figure 8. Additionally, it may be observed that the circular paths presented with a larger variation in image matching feature density, relative to adaptive paths generating images with comparable average quality.

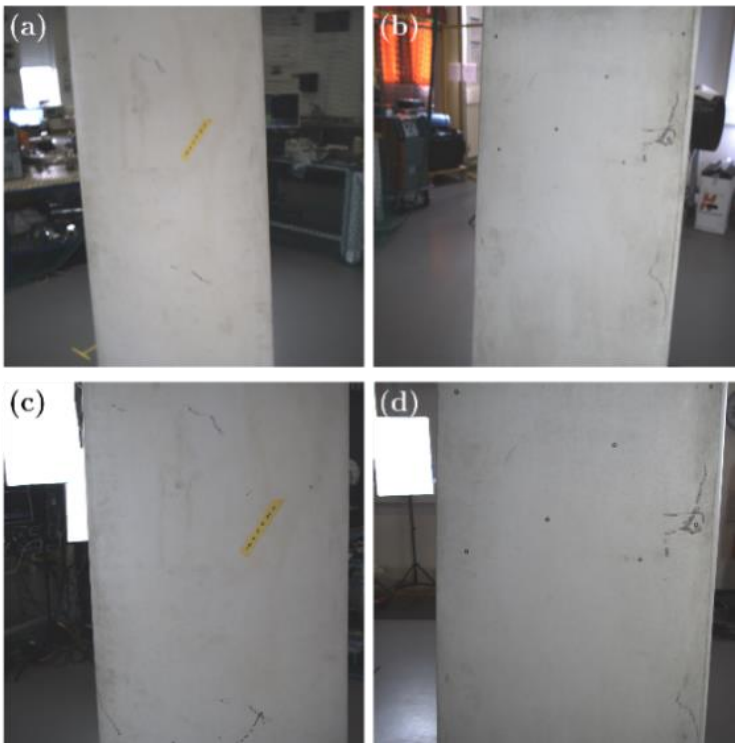

Figure 14 Raw images captured during inspection of similar blade sections. (a)(b) are captured during the inspection with the circular path. (c)(d) are captured during the inspection with the laser-based path

Deviation maps of the model reconstructed from images gathered with the pre-planned path and laser-based paths are shown in Figure 15. The reconstruction errors from each of the two trajectories are listed in Table 3.

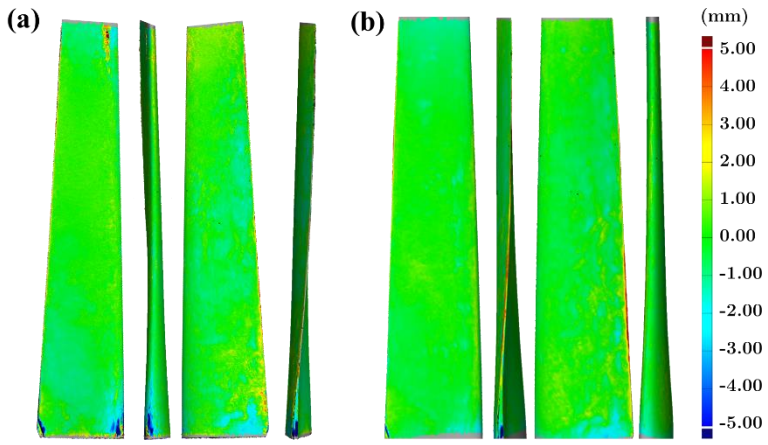

Figure 15 Deviation maps of the model reconstructed based on the images captured from (a) circular path (b) laser-based path

Table 3 Reconstruction errors from the inspection with the circular flight path and laser-based path

Path Type	Mean Error (mm)	Standard Deviation (mm)	Peak-to-peak Error (mm)
Circular (30 ms shutter time, 600 mm closest approach, Light = 200 lx)	0.3853	1.56	13.56
Laser-based (30 ms shutter time, 600 mm laser-controlled standoff distance, Light = 200 lx)	0.3098	1.29	5.09

Comparison of results shows that the inspection with laser scanner had more accurate alignments and smaller measurement error in terms of both standard deviation and peak-to-peak than the pre-planned circular trajectory. The disparity between errors in different paths emphasises that the result from the laser scanner path granted a smoother surface and more precise reconstructed mesh. The standard deviation and mean error were improved by approximately 20%, while the peak-to-peak errors were reduced by a factor of 2.7. Compared with the pre-planned flight path, the laser scanner path-adaptation ensured that the UAV deployed the photogrammetric measurement at a proper standoff distance in accordance with the camera's focal length. The path with the laser scanner therefore provides better focusing of the camera so that more detailed features are resolved within the images. Additionally, some differences are notable in the textures of reconstructed models from the two flight paths. The reconstructed model from the pre-planned path has more distorted features on the mesh because the raw images contain degradations caused by focal blur, as shown in Figure 16 (a)-(e). By way of comparison, Figure 16 (f)-(j) display the textures of the model reconstructed from the images acquired during the inspection that used the laser-based path. The textures on the laser-based model contain sharper and more detailed features. It may thus be surmised that adaptive path correction using the laser data is an effective strategy to minimise the negative impact of the focal blur in the final inspection results.

5.2. Standoff Distance

Standoff distance between the target object and UAV onboard camera impacts the details of texture, depth of field and image quality. These parameters relate to the reconstruction process and model accuracy. During an inspection, a greater standoff distance provides a larger depth of field and allows the object to remain more suitably in focus with similar UAV position variation. In turn, the greater standoff distance also offers the camera a broader field of view to capture larger areas of a structure's surface in a single image. Thus, the UAV requires a shorter time to inspect the complete structure, reducing the need for multiple flights and increasing inspection efficiency. Additionally, the image processing time during reconstruction is reduced because fewer images are generated during the shorter inspection. However, compared with an inspection conducted with a small standoff, significant texture detail is sacrificed as the result of lower pixel density and diminished ability to spatially resolve features; aspects of critical importance to the quality of the inspection process. An optimal point between speed and accuracy must therefore be found.

To directly quantify the impact of standoff on reconstruction accuracy, successive inspections were undertaken at three standoff distances (400 mm, 600 mm and 800 mm), with the camera focusing optimised according to the corresponding distance. In all cases, the standoff distance was maintained utilising measurements from the laser scanner. The experiments were undertaken with the supplementary external lighting, permitting the camera shutter time to be set at 30 ms. The resultant reconstruction accuracies from the models generated at each of the three standoff distances are listed in Table 4. The image qualities attainted at the three standoff distances are, again, plotted in Figure 8.

Table 4 Reconstruction errors from the inspection with three standoff distances (Distance is maintained by the laser scanner)

	Mean Error (mm)	Standard Deviation(mm)	Peak-to-peak Error (mm)
400 mm standoff distance (Light = 200 lx)	0.2442	0.92	4.30
600 mm standoff distance (Light = 200 lx)	0.3098	1.29	5.09
800 mm standoff distance (Light = 200 lx)	0.3962	1.30	9.13

The reconstruction errors from different standoff distances highlight the trade-off between the reconstruction accuracy and UAV standoff distance. As shown by the peak-to-peak error, standard deviation and mean error respectively, the model using 400 mm standoff distance is more accurate, smoother and better aligned with the ground-truth model than that using the 800 mm standoff. The mean and peak-to-peak errors were reduced by a factor of two. The standard deviation shows how the reconstructed surface became smoother with the reduction of standoff distance.

Figure 8 illustrates how the image sets taken from 400 mm standoff distance exhibited large variation in image quality expressed in terms of the matching feature density metric. Additionally, it highlights a relationship between the image quality variation and UAV standoff distance. The shorter standoff distance entails that more details are taken from the surface of the inspection object, improving reconstruction quality. However, the closer proximity also causes an exponentially narrower depth of field of the camera, requiring a tighter control of UAV position and leading to additional focal blurring, as discussed in Section 4.3, manifesting in Figure 8 as increased variation in image quality. Furthermore, the UAV was observed to be unstable when flying at 400 mm standoff owing to near-structure aerodynamic effects, causing further motion-based blur to appear in the images. In progressing from 800 mm to 600 mm and 400 mm standoff distance, the standard deviation in the flight path changed from 23.96 mm to 24.55 mm and 29.87 mm. Again, this indicates an exponential degradation that imposes limits on the minimum standoff distance where at a UAV photogrammetric inspection can be safely and practically conducted.

6. Discussion

It has been shown that the lighting conditions, motion blur and focal blur are major parameters that negatively impact the accuracy of UAV based photogrammetric inspection. The detrimental effects of these parameters, however, can be lessened by the use of appropriate experimental setups. External lighting, or a brighter outdoor environment, and longer shutter time introduce more illuminance to the camera, which improves image brightness and quality. As presented in Figure 8, these improvements increased the reconstruction accuracies and significantly reduced the model errors. The compromise between shutter time and motion blur highlighted in Section 4.2, however, remains pertinent and must be considered when planning inspections. Increased environmental light levels should always take precedence over longer exposure times so as to minimise motion blurring effects. The comparisons between manual inspection and autonomous inspection show the motion blur increased the reconstruction error by a factor of two in the longest exposures investigated. Additional deformation is found in the Focal blur introduced due to the narrow depth of field during close-range inspection. Application of a laser ranging scanner demonstrated the ability to maintain the desired standoff distance and significantly reduce the errors observable in the reconstructed models and associated data. With the laser scanner adaptive inspection path, the UAV kept an optimal position relative to the object's surface, holding this target within the camera's depth of field. Here, captured images were sharper and had better quality under the matching feature

density metric, as shown in Figure 8. The reconstructed model, in this case, is more accurate than the pre-planned path and presents better-detailed textures.

In terms of flight parameters, the reconstruction error was found to reduce with shorter standoff distances, which improve the spatial resolution and provide the capability for the camera to capture more detailed surface information. Although the inspection with 400 mm standoff distance had the most accurate reconstruction model in this paper, it should be noted that the UAV flight was notably less stable throughout the inspection due to the near-surface aerodynamic effects from the wind turbine blade structure. The risk of collision with the inspection target is thus greatly increased when approaching as closely outside a laboratory environment. Compared with the inspection at 800 mm, the model from 600 mm standoff was more accurate and had a smaller peak-to-peak error. Therefore, in light of a compromise between safety and reconstruction accuracy, 600 mm is identified as the optimal standoff distance for the UAV photogrammetric inspections conducted in the manner described herein.

During outdoor inspections, a better environmental brightness can be leveraged to extend the camera depth of field via utilisation of a smaller camera aperture, resulting in the images with less focal blur. However, as shown in Figure 10, the image had the best quality at the camera focal point (in that case 600 mm). The reduced aperture size only serves to widen the depth of field wherein acceptable images may be captured. While it is still necessary to perform the inspection with a smaller standoff to obtain the spatial resolution required for more detailed features even with an extended depth of field, a smaller aperture will reduce the level of UAV position control required and make better allowance for environmental position disturbances commonly induced by wind outdoors. Maintaining a relatively constant standoff is, thus, still necessary for outdoor inspections but presents additional challenges. Typical outdoor navigation systems employed are less accurate than the indoor system (e.g. the error from Differential GPS positioning systems can reach to 0.22 m [50], compared to the millimetre scale errors of the Vicon tracker). The position noise in such sensors can lead to flight instability and introduce the motion blur without proper compensation, further increasing the limit on minimum standoff distance. As described in Section 4.2, such impacts can be lessened by the use of shorter camera exposure time, since daylight can introduce more illumination on the camera in certain conditions. Such camera setting adjustments require the balance between the camera shutter speed and aperture size. Hence, the findings from this paper may be applied during the outdoor inspections and used to inform inspection configuration and planning in the presence of poorer environmental conditions. In addition, the laser scanner herein offers real-time adaptive corrections of less accurate navigation systems, and thereby represents a means through which the standoff to the target object can be maintained within the camera depth of field during outdoor inspections.

Typical types of wind turbine blade damage [39], [40], including edge crushing, surface imperfections, early stage leading edge erosion and other edge damage, were clearly reconstructed in the 3D model. These surface failures are visible to varying degrees in the circular inspection (Figure 16 (a)-(e)) and laser-based inspection (Figure 16 (f)-(j)), but are far clearer in Figure 16 (f)-(j). The reconstructed image qualities of the naturally occurring (Figure 16 (f)-(h)) and artificial visual features (Figure 16 (i)-(j)) were improved by 17.64% and 2.84% respectively, quantified by using the blur metric described in [49]. The differences in improvement between the naturally occurring and artificial visual features were caused by their relative contrast versus the background material. In the naturally occurring defects, coloration is similar to the undamaged material and the features are finer in structure than those of the artificial markers. Natural defects are therefore more sensitive to the effects of focal blurring arising from the change in path. Another contributing factor may be found in the position of the features around the blade perimeter. As the natural and artificial features have different locations, they experience different changes in the level of focal blurring when the flight path is altered from circular to laser based. As is shown in Figure 11, the areas furthest from the blade edges experience the greatest improvement in flightpath offset and consequently are subject to the largest changes in image quality due to focal blur. Notably, as per Figure 16 (f), the transverse crack on the blade trailing edge is clearly observable in the 3D reconstruction that used the laser-based path, while it is hard to identify in the model that used the circular path (Figure 16 (a)) and may be overlooked in an inspection report. It may thus be surmised that adaptive path correction using the laser data is an effective strategy to minimise the negative impact of the focal blur in the final inspection results.

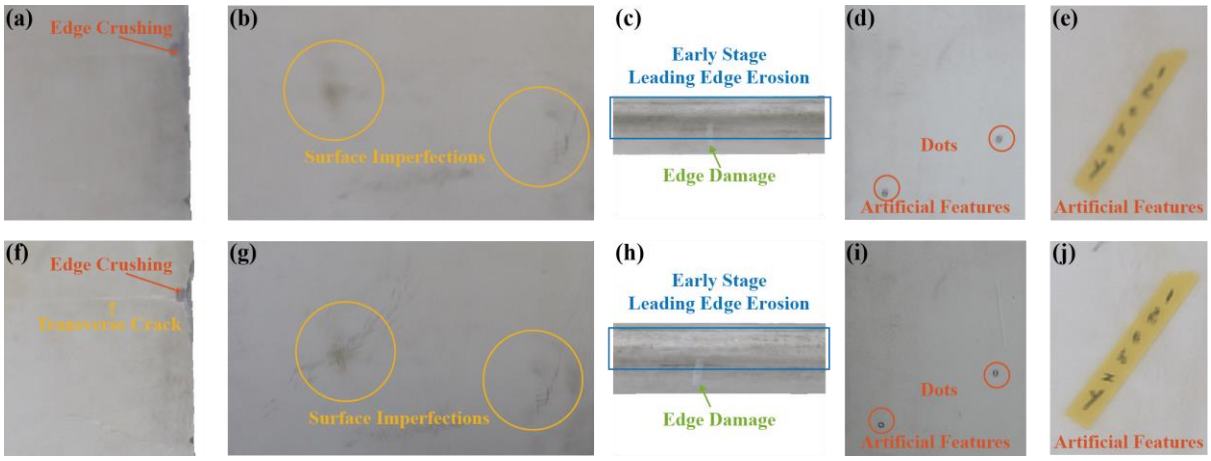

Figure 16 An illustrative comparison of surface textures in the photogrammetric model reconstructed from images acquired using the circular flight path (a)-(e) and adaptive laser-based flight path (f)-(j).

7. Conclusions

In summary, this paper presented an autonomously controlled UAV system utilising a machine vision camera and miniature laser scanner. The integrated system was deployed to undertake photogrammetric inspection of a wind turbine blade section within a laboratory environment. Inspection results are presented as a 3D reconstructed model generated from the images taken during the UAV flight. Using this system, the mean error of the reconstructed model under optimised conditions is below 0.25 mm, the peak-to-peak error is less than 4.3 mm and the standard deviation is below 0.92 mm when compared with a ground-truth, metrology grade reconstruction. This is intended to serve as a bounding limit on expectations of reconstruction accuracy when employing similar systems under suboptimal conditions outside the laboratory. This paper further analyses and quantifies the impacts of different parameters on the photogrammetric inspection accuracy when carried out using the UAV agent with regard to the quality of the final model and visibility of these features. Particular examination is given to the detrimental effects of lighting conditions, motion blur and focal blur. Based on the aforementioned results, the following observations were made:

- Instances of wind turbine blade damage (i.e. edge crushing, surface imperfections, transverse cracking, early stage leading edge erosion and general edge damage) were clearly observed in the textured 3D reconstruction profiles, indicating the utility of the successful inspection process.
- UAV motion during exposure causes blurring, increasing the reconstruction standard deviation and peak-to-peak error by a factor of two when compared to the ground truth. Informed selection of camera settings and tighter flight control system may compensate for this to a limited extent.
- The laser scanner maintained the standoff distance within the camera's depth of field to reduce the focal blur, introduced due to the narrow depth of field. Consequently, significant error reductions (by a factor of 2.7) were observable in the reconstructed models and associated data.
- Employing shorter standoff distances reduced the reconstruction error and provided surface textures with improved spatial resolution of defect features under consistent imaging hardware. However, the near-surface aerodynamic challenges destabilise the UAV during close proximity inspections imposing a practical limit.
- Over the range of parameter values studied, the poorest scenario was observed to cause a degradation in reconstruction error by a factor of 13 versus the optimal.

Overall, despite the negative influences these parameters (lighting conditions, motion blur and focal blur) have on reconstruction errors, it is shown herein that a well-designed UAV flight path with an active correction mechanism and appropriate experimental setup can mitigate their impact on reconstruction accuracy and enable

the return of informative inspection reports. The findings from this paper provide a benchmark for reconstruction quality and the impact of environment effects during photogrammetric inspections, offering practical insight towards their mitigation in future airborne photogrammetric research.

Funding

This work was supported by the ESPRC Autonomous Inspection in Manufacturing & Remanufacturing (AIMaReM) project (EP/N018427/1) and Pressure Profile Systems, Inc. (PPS).

Declarations of interest: none.

References

[1] S. Jordan *et al.*, "State-of-the-art technologies for UAV inspections," *IET Radar, Sonar Navig.*, vol. 12, no. 2, pp. 151–164, Jan. 2018.

[2] H. F. Zhou, H. Y. Dou, L. Z. Qin, Y. Chen, Y. Q. Ni, and J. M. Ko, "A review of full-scale structural testing of wind turbine blades," *Renew. Sustain. Energy Rev.*, vol. 33, pp. 177–187, 2014.

[3] J. Sabel, "Optical 3D motion measurement," in *In Instrumentation and Measurement Technology Conference, 1996. IMTC-96. Conference Proceedings. Quality Measurements: The Indispensable Bridge between Theory and Reality., IEEE*, 1996, vol. 1, pp. 367–370.

[4] J. T. Johnson, S. Hughes, and J. van Dam, "A Stereo Videogrammetry System for Monitoraing Wind Turbine Blade Surfaces during Structural Testing," in *ASME Early Career Technical Conference*, 2009, vol. 8, pp. 1.1-1.10.

[5] T. Lundstrom, J. Baqersad, C. Niezrecki, and P. Avitabile, "Using high-speed stereophotogrammetry techniques to extract shape information from wind turbine/rotor operating data," *Conf. Proc. Soc. Exp. Mech. Ser.*, vol. 6, pp. 269–275, 2012.

[6] D. Roca, S. Lagüela, L. Díaz-Vilariño, J. Armesto, and P. Arias, "Low-cost aerial unit for outdoor inspection of building façades," *Autom. Constr.*, vol. 36, pp. 128–135, 2013.

[7] V. N. Nguyen, R. Jenssen, and D. Roverso, "Automatic autonomous vision-based power line inspection: A review of current status and the potential role of deep learning," *Int. J. Electr. Power Energy Syst.*, vol. 99, pp. 107–120, 2018.

[8] R. A. Clark *et al.*, "Autonomous and scalable control for remote inspection with multiple aerial vehicles," *Rob. Auton. Syst.*, vol. 87, pp. 258–268, 2017.

[9] D. Lattanzi and G. R. Miller, "3D Scene Reconstruction for Robotic Bridge Inspection," *J. Infrastruct. Syst.*, vol. 21, no. 2, p. 04014041, 2015.

[10] J. Seo, L. Duque, and J. Wacker, "Drone-enabled bridge inspection methodology and application," *Autom. Constr.*, vol. 94, pp. 112–126, 2018.

[11] L. Duque, J. Seo, and J. Wacker, "Bridge Deterioration Quantification Protocol Using UAV," *J. Bridg. Eng.*, vol. 23, no. 10, 2018.

[12] L. Duque, J. Seo, and J. Wacker, "Timber Bridge Inspection Using UAV," *Struct. Congr. 2018 Bridg. Transp. Struct. Nonbuilding Struct. - Sel. Pap. from Struct. Congr. 2018*, vol. 2018-April, pp. 186–196, 2018.

[13] J. Seo, J. P. Wacker, and L. Duque, "Evaluating the Use of Drones for Timber Bridge Inspection.," *Gen. Tech. Rep. - For. Prod. Lab. USDA For. Serv.*, p. 1.

[14] L. Duque, J. Seo, and J. Wacker, "Synthesis of Unmanned Aerial Vehicle Applications for Infrastructures," *J. Perform. Constr. Facil.*, vol. 32, no. 4, 2018.

[15] S. S. Mansouri, C. Kanellakis, E. Fresk, D. Kominiak, and G. Nikolakopoulos, "Cooperative coverage path planning for visual inspection," *Control Eng. Pract.*, vol. 74, pp. 118–131, 2018.

[16] L. Wang and Z. Zhang, "Automatic Detection of Wind Turbine Blade Surface Cracks Based on UAV-

Taken Images," *IEEE Trans. Ind. Electron.*, vol. 64, no. 9, pp. 7293–7309, 2017.

[17] S. Jung, J. U. Shin, W. Myeong, and H. Myung, "Mechanism and system design of MAV(Micro Aerial Vehicle)-type wall-climbing robot for inspection of wind blades and non-flat surfaces," in *ICCAS 2015 - 2015 15th International Conference on Control, Automation and Systems, Proceedings*, 2015, pp. 1757–1761.

[18] M. Stokkeland, K. Klausen, and T. A. Johansen, "Autonomous visual navigation of Unmanned Aerial Vehicle for wind turbine inspection," in *2015 International Conference on Unmanned Aircraft Systems, ICUAS 2015*, 2015, pp. 998–1007.

[19] N. Snavely, S. M. Seitz, and R. Szeliski, "Photo tourism," in *ACM SIGGRAPH 2006 Papers on - SIGGRAPH '06*, 2006, p. 835.

[20] Y. Furukawa and J. Ponce, "Accurate, dense, and robust multiview stereopsis," *IEEE Trans. Pattern Anal. Mach. Intell.*, vol. 32, no. 8, pp. 1362–1376, 2010.

[21] J. Engel, T. Schops, and D. Cremers, "LSD-SLAM: Large-Scale Direct monocular SLAM," *Lect. Notes Comput. Sci. (including Subser. Lect. Notes Artif. Intell. Lect. Notes Bioinformatics)*, vol. 8690 LNCS, no. PART 2, pp. 834–849, 2014.

[22] R. a N. Rse, "KinectFusion : Real-Time Dense Surface Mapping and Tracking," 2013.

[23] A. Rajput, E. Funk, A. Börner, and O. Hellwich, "A Regularized Volumetric Fusion Framework for Large-Scale 3D Reconstruction," *ISPRS J. Photogramm. Remote Sens.*, vol. 141, pp. 124–136, 2018.

[24] M. Keller, D. Lefloch, M. Lambers, S. Izadi, T. Weyrich, and A. Kolb, "Real-time 3D reconstruction in dynamic scenes using point-based fusion," in *Proceedings - 2013 International Conference on 3D Vision, 3DV 2013*, 2013, pp. 1–8.

[25] Q. Peng, L. Tu, K. Zhang, and S. Zhong, "Automated 3D scenes reconstruction using multiple stereo pairs from portable four-camera photographic measurement system," *Int. J. Opt.*, vol. 2015, p. 1?9, 2015.

[26] C. Fritz, M. D. Willis, and G. Tosello, "Reconstructing Paleolithic cave art: The example of Marsoulas Cave (France)," *J. Archaeol. Sci. Reports*, vol. 10, pp. 910–916, 2016.

[27] S. Grzonka, G. Grisetti, and W. Burgard, "A fully autonomous indoor quadrotor," *IEEE Trans. Robot.*, vol. 28, no. 1, pp. 90–100, 2012.

[28] G. Morgenthal and N. Hallermann, "Quality Assessment of Unmanned Aerial Vehicle (UAV) Based Visual Inspection of Structures," *Adv. Struct. Eng.*, vol. 17, no. 3, pp. 289–302, 2014.

[29] J. O'Connor, M. J. Smith, and M. R. James, "Cameras and settings for aerial surveys in the geosciences: Optimising image data," *Prog. Phys. Geogr.*, vol. 41, no. 3, pp. 325–344, Mar. 2017.

[30] Ascending Technologies, "AscTec Firefly Technical Data," *Online Webpage*, 2015. [Online]. Available: http://wiki.asctec.de/display/AR/AscTec+Firefly#AscTecFirefly-TechnicalData. [Accessed: 07-Nov-2018].

[31] FILR, "Chameleon3 5.0 MP Color USB3 Vision (Sony IMX264)," *Online Webpage*, 2017. [Online]. Available: https://eu.ptgrey.com/chameleon3-50-mp-color-usb3-vision-sony-imx264-3. [Accessed: 03-Nov-2018].

[32] Computar, "M0824-MPW2," *Online Webpage*, 2017. [Online]. Available: https://computar.com/product/1331/. [Accessed: 31-Oct-2018].

[33] Hokuyo, "Scanning Laser Range Finder URG-04LX Specifications," *Online Webpage*, 2005. [Online]. Available: https://www.hokuyo-aut.jp/dl/Specifications_URG-04LX_1513063395.pdf. [Accessed: 31-Oct-2018].

[34] S. Bouabdallah, P. Murrieri, and R. Siegwart, "Design and control of an indoor micro quadrotor," in *IEEE International Conference on Robotics and Automation, 2004. Proceedings. ICRA '04. 2004*, 2004, pp. 4393-4398 Vol.5.

[35] R. Summan *et al.*, "Spatial calibration of large volume photogrammetry based metrology systems," *Meas. J. Int. Meas. Confed.*, vol. 68, pp. 189–200, 2015.

[36] P. Merriaux, Y. Dupuis, R. Boutteau, P. Vasseur, and X. Savatier, "A study of vicon system positioning performance," *Sensors (Switzerland)*, vol. 17, no. 7, 2017.

[37] C. N. Macleod, R. Summan, G. Dobie, and S. G. Pierce, "Quantifying and improving laser range data

when scanning industrial materials," *IEEE Sens. J.*, vol. 16, no. 22, pp. 7999–8009, 2016.

[38] Gaia-Wind, "Gaia-Wind," *Online Webpage*, 2018. [Online]. Available: http://www.gaia-wind.com/. [Accessed: 10-Nov-2018].

[39] S. Ataya and M. M. Z. Ahmed, "Damages of wind turbine blade trailing edge: Forms, location, and root causes," *Eng. Fail. Anal.*, vol. 35, pp. 480–488, 2013.

[40] H. M. Slot, E. R. M. Gelinck, C. Rentrop, and E. Van der Heide, "Leading edge erosion of coated wind turbine blades: Review of coating life models," *Renew. Energy*, vol. 80, pp. 837–848, 2015.

[41] Agisoft LLC, "Agisoft PhotoScan User Manual: Professional Edition, Version 1.4," 2018. [Online]. Available: http://www.agisoft.com/pdf/photoscan-pro_1_4_en.pdf. [Accessed: 07-Nov-2018].

[42] GOM, "ATOS Triple Scan," 2015. [Online]. Available: http://www.gom.com/metrology-systems/system-overview/atos-triple-scan.html. [Accessed: 07-Nov-2018].

[43] J. J. Koenderink and A. J. van Doorn, "Affine structure from motion," *J. Opt. Soc. Am. A*, vol. 8, no. 2, p. 377, 1991.

[44] G. Dobie, R. Summan, C. MacLeod, and S. Gareth Pierce, "Visual odometry and image mosaicing for NDE," *NDT E Int.*, vol. 57, pp. 17–25, 2013.

[45] M. P. Christiansen, M. S. Laursen, R. N. Jørgensen, S. Skovsen, and R. Gislum, "Designing and testing a UAV mapping system for agricultural field surveying," *Sensors (Switzerland)*, vol. 17, no. 12, 2017.

[46] L. Kneip, F. Tache, G. Caprari, and R. Siegwart, "Characterization of the compact Hokuyo URG-04LX 2D laser range scanner," in *2009 IEEE International Conference on Robotics and Automation*, 2009.

[47] R. Jain, R. Kasturi, and B. Schunck, *Machine Vision*. McGraw-Hill Education, 1995.

[48] Stephen H. Westin, "ISO 12233 Test Chart," *Online Webpage*, 2010. [Online]. Available: https://www.graphics.cornell.edu/~westin/misc/res-chart.html. [Accessed: 10-Nov-2018].

[49] F. Crete, T. Dolmiere, P. Ladret, and M. Nicolas, "The blur effect: perception and estimation with a new no-reference perceptual blur metric," p. 64920I, 2007.

[50] L. S. Monteiro, T. Moore, and C. Hill, "What is the accuracy of DGPS?," *J. Navig.*, vol. 58, no. 2, pp. 207–225, 2005.